3D Electron diffraction on nanoparticles: minimal size and associated dynamical effects

Erica Cordero Oyonarte, Luca Rebecchi, Saleh Gholam, Moussa Faye Diouf, Edma Bigard, Valérie Pralong, Carmelo Prestipino, Ilka Kriegel, Ana Castellanos-Aliaga, Joke Hadermann, et al.

3D Electron Diffraction on Nanoparticles: Minimal Size and Associated Dynamical Effects

Erica Cordero Oyonarte [†], Luca Rebecchi [‡,§], Saleh Gholam [∥], Moussa D Faye Diouf [⊥,#], Edma Bigard [†], Valérie Pralong [†], Carmelo Prestipino [†], Ilka Kriegel [‡], Ana Castellanos-Aliaga [¶], Joke Hadermann [∥], Mauro Gemmi [⊥], Lukas Palatinus [▽], Jasper R Plaisier [○], Philippe Boullay [†,*]

Abstract

Over the past decade, advances in electron diffraction (ED) have significantly improved the determination and refinement of crystal structures, making it a viable alternative to traditional X-ray diffraction (XRD), especially for very small volumes, such as nanoparticles (NPs). This work evaluates the application of advanced 3D ED techniques to the analysis of isolated NPs, focusing on their efficacy and limitations in terms of crystal size and accuracy of results. Our investigation begins by addressing the challenges of obtaining 3D ED data for NPs, including sample preparation, instrument capabilities, and the choice of 3D ED methods. We find that 3D ED can provide highly accurate structure refinements for crystals in the 50–100 nm range and is also effective for the analysis of NPs as small as 10 nm. While kinematical approximations often provide accurate refinements similar to those obtained from powder XRD, the accuracy depends on the specific data set and may not always align with traditional reliability indicators. Our study shows that dynamical scattering effects, even in tiny crystals, challenge the assumption that they are negligible in thin crystal scenarios. Addressing these effects through full dynamical refinement significantly improves the accuracy and reliability of the structure determination. This report suggests a paradigm shift in viewing dynamic scattering effects not as mere obstacles but as opportunities to explore crystal structures in greater detail on smaller scales. By embracing these complexities, 3D ED can provide precise and reliable structural insights that are critical to the advancement of nanotechnology and materials science.

Keywords: electron diffraction, crystallography, electron microscopy, oxide nanoparticles, dynamical refinement

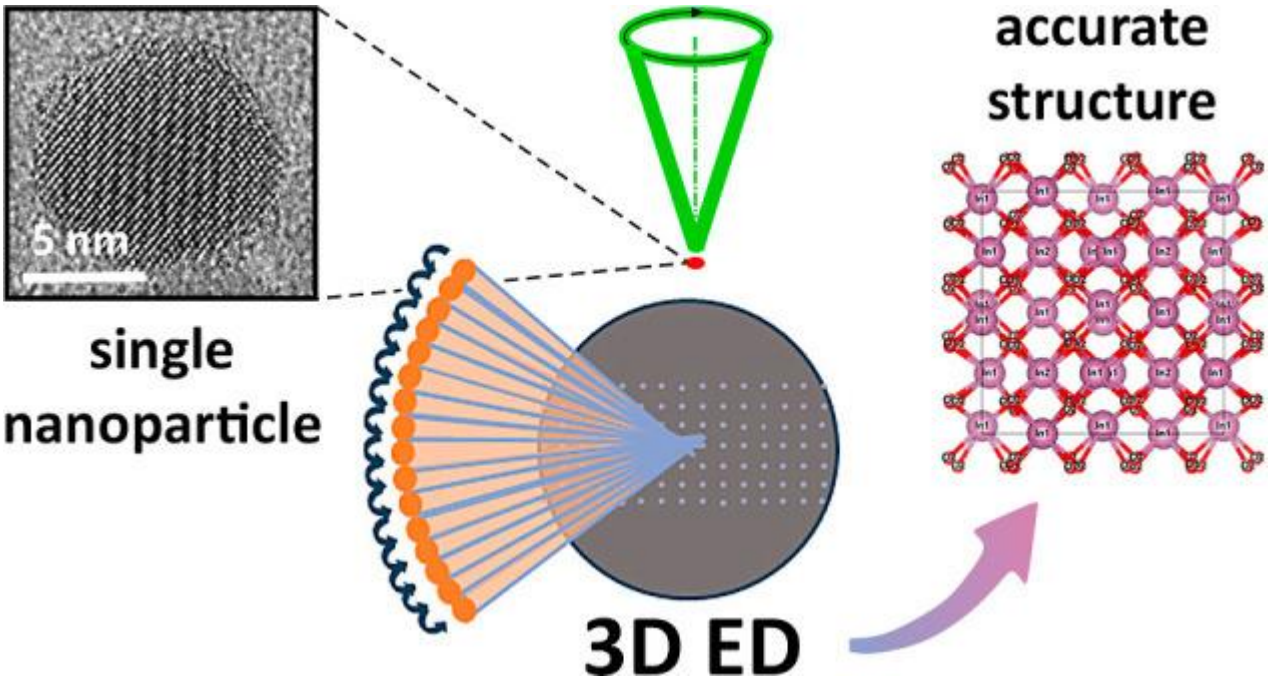

Nanoparticles (NPs) are of significant interest for a wide range of applications due to their unique properties and potential benefits. Key reasons for this interest include their size-dependent properties (optics and electronics), high surface area and enhanced reactivity (catalysis), improved mechanical and thermal properties (lubricants and composites), targeted drug delivery (healthcare), energy conversion and storage (cells and batteries), and environmental benefits (filtration and purification). Research on NPs drives advances in all sectors, from healthcare to energy and electronics, leading to improved materials, more efficient energy solutions, and better medical treatments. These innovations benefit everyday life, offering more efficient and safer products for a sustainable environment. In relation to their properties, knowledge of the crystallographic structure of NPs is essential to reveal the origin of their unique characteristics and design new functional materials. While NPs are likely to possess simple and already known crystal structures, access to this information is not always so straightforward. In cases where, due to size-dependent effects, the crystal structure cannot be merely extrapolated from already known crystal structures, a so-called ab initio structure solution is required. As studies involving nanomaterials have a trend to develop toward more complex systems, potentially leading to more complex or unknown crystal structures, the need for accurate structure analysis of NPs will grow.

Single crystal X-ray diffraction (SCXRD) is the most common method for the ab initio determination of crystal structures. However, SCXRD has significant limitations for NPs due to their size. NPs are typically defined as nanosized crystals with at least one dimension (length, width, or height) within the nanometer range (typically below 100 nm). For this study, NPs are considered to have all dimensions below 100 nm, i.e., volumes below 0.001 μm^3. NPs are generally well below the detection limit of the best-performing laboratory single-crystal diffractometer (a few μm^3), even considering synchrotron radiation as a source. Because NPs may have a relatively small number of unit cells, obtaining a diffraction pattern with sufficient

intensity for analysis is challenging. To address this, XRD data can be collected from an assembly of NPs to enhance the scattered signal. This approach, used in powder XRD (PXRD), can be useful for extrapolating NP structures from larger crystals (further referred to as “bulk structure”). While simple structures can often be resolved easily with PXRD, the technique can be of limited use for complex structures, mixtures, or small particles due to significant peak broadening and overlap, which can hinder unambiguous identification.

Electron diffraction (ED) appears to be more suitable for accurately studying the crystal structure of a single NP. Electrons interact more strongly with matter than X-rays, making them ideal for diffraction experiments with volumes below a few μm^3. This advantage has been increasingly exploited since the appearance of so-called 3D electron diffraction (3D ED) approaches. 3D ED aims at obtaining a three-dimensional reconstruction of the reciprocal space of a crystalline particle by recording a series of nonoriented ED patterns. This approach and the associated crystallographic tools represented a paradigm shift when they were first proposed. By collecting as many reflections as possible from randomly oriented diffraction patterns obtained simply by tilting the crystal, without focusing on dense zone-axis patterns where multiple scattering is most pronounced, electron crystallography found a path toward quantitative analysis of diffracted intensities. In fact, nowadays two key acquisition approaches have emerged, namely precession-assisted 3D ED and continuous-rotation 3D ED (Figure). What these two approaches have in common is that they allow data collection in which measured intensities are integrated over a certain angular range. The result is a better measure of intensities, enabling their use for structural analyses within the framework of the kinematic approximation with the crystallographic tools classically used in XRD. This is what has enabled these approaches to find users and develop. This intensity integration is also essential if we are to achieve accurate structure refinements that consider both diffraction geometry and dynamical scattering effects using so-called dynamical refinements. , What differentiates these two approaches is the way that the intensities are collected and integrated. For precession-assisted 3D ED (a.k.a., precession-assisted electron diffraction tomography□PEDT), the sample is rotated/tilted sequentially (0.5° to 1°), and a precession ED pattern is recorded at each step (preferably with a semiangle larger than half of the tilt step). Here, the precession motion ensures the integration. For continuous rotation 3D ED (a.k.a. under the acronyms cRED or microED), the sample rotates continuously, and ED patterns are recorded on the fly. Here, the integration (typically over a few tenths of a degree) is performed by adjusting the exposure time to the rotation speed. Another major difference is the duration of 3D ED data collection. Step by step, for an angular range of 90°, a “fast” acquisition will be around 10 min; in continuous rotation, this can be less than a minute.

1.

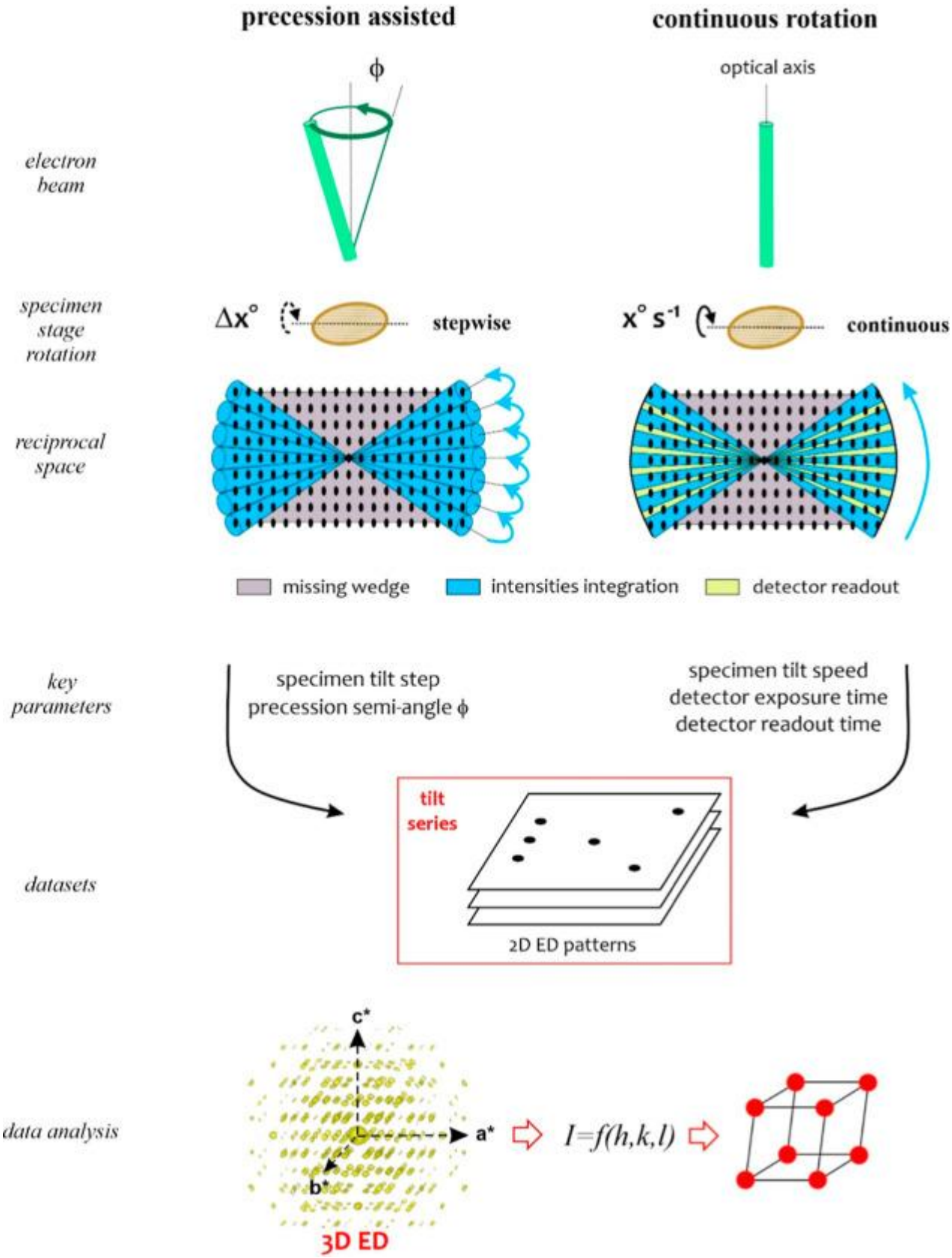

Schematic representation of the two most common approaches to acquire ED tilt series. Both approaches provide integrated diffracted intensities thanks to the electron beam precession motion (precession-assisted 3D ED) or the rotation of the sample while acquiring ED patterns (continuous rotation 3D ED). The ED tilt series can be used to reconstruct a part of the

reciprocal lattice to obtain the diffracted intensities as a function of *hkl* indexes and use them for structure solution and refinement.

Pioneering studies showed the strong potential of 3D ED for analyzing nanomaterials, applied to a few NPs. − The question remains regarding the size limit at which 3D ED data can still be collected with sufficient quality for structure solution and, ideally, accurate structure refinement. What are the most suitable experimental setups for collecting 3D ED data on NPs, and what challenges might arise during this process? What detailed structural information can be extracted through dynamical refinements, which is a central aspect of this study? While it is generally accepted that reducing sample thickness and/or crystal size minimizes the impact of multiple scattering, the question still persists: can an accurate structural analysis of NPs be performed using a refinement based solely on the kinematic theory approximation? This review aims at answering these questions and provides an overview of what can be achieved with 3D ED on isolated NPs, with a focus on inorganic NPs.

Results and Discussion

TiO_2 Brookite Nanorods

Brookite was chosen as an example of a "large" NP for which 3D ED data collection should be relatively easy. The term "relatively" refers to the prerequisites and limitations concerning beam size and the difficulty of tracking NP motion (see Materials and Methods). Brookite nanorods are also stable under the beam with no diffraction decay over time or change in the particle morphology. All data sets were recorded at room temperature. For this sample, experimental constraints are less stringent and should be achievable for a wide range of instrumental configurations. To test this a priori, three different instruments were used: FEI Tecnai G2 X-TWIN F20 (University of Antwerp□UA), ZEISS Libra 120 (Istituto Italiano di Tecnologia, IIT), and JEOL F200 (CRISMAT□CNRS). On these instruments (see details in the section Materials and Methods), the typical beam size diameters used for data acquisition were 300, 600, and below 100 nm, respectively. The data acquisition mode was precession-assisted step-by-step 3D ED for CNRS and continuous rotation 3D ED for UA and IIT.

Some key parameters obtained with representative data sets acquired with the different experimental setups are shown in Table . To check the accuracy of the 3D ED structure refinements, these results are compared with reference structures found in the literature and synchrotron PXRD (see Materials and Methods) obtained from the same synthesis. This comparison is performed using the COMPSTRU utility of the Bilbao Crystallographic Server, which allows us to obtain the average (av. dist. in Table) and maximal deviation (max. dist. in Table) on atomic positions. Refinements in the kinematic approximation are similar to those performed with SCXRD data except for the use of scattering factors specific to ED. Dynamical refinements, on the other hand, are specific, and for details, please refer to the literature for precession-assisted 3D ED , and continuous rotation 3D ED. In the context of this study, we would like to draw attention to a few points and clarify some of the numbers you will find in Table . As dynamical refinements are frame-based, it implies that there is no averaging of symmetry-equivalent reflections, as done in kinematical refinements. This is the reason why the number of measured and observed reflections is much larger in the case of dynamical

refinements. There is also a significant increase in the number of refined parameters compared to kinematical refinements, as the refinement of a scale factor is carried out for each ED frame in the tilt series.

1. Structure Refinement Results Obtained from 3D ED Data Recorded under Different Acquisition Conditions for Brookite .

	UA	IIT	CNRS-01	CNRS-02	CNRS-03	CNRS-04
Tilt Range (°)	[-45, +35]	[-55.5, +61]	[-48, +50]	[-50, 54]	[-44, +38]	[-50, +60]
Exp. per frame (s)	0.5	0.5	0.5	0.5	1.5	1
Tilt step per frame (°)	0.2	1	1	2	2	1.5
PED / Integ. Angle (°)	- / 0.1	- / 0.5	1.2 / -	1.3 / -	1.2 / -	1.3 / -
Cumul. Cover. *(sinθ/λ=0.7 Å^{-1})*	85.7	99.6	87.1	97.2	71.2	95.2
Averaged Refl. all/obs.	307/180	361/256	328/312	355/259	253/235	341/ 325
Redundancy	3.59	4.140	4.46	4.23	4.35	4.81
Rint (from PETS)	10.7	17.00	16.2	16.8	12.0	16.2
Number of refined parameters	13	13	13	13	13	13
Robs	14.9	14.75	17.03	18.52	17.32	19.53
Rall	20.03	17.92	17.80	22.07	18.02	19.97
av. dist. (Å)	0.0442	0.0185	0.0108	0.0132	0.0323	0.0474
max. dist. (Å)	0.0917	0.0318	0.0162	0.0224	0.0388	0.0798
Refl. all/obs.	766/551	1425/718	3611/3110	1985/1891	1695/1507	2682/2184
Number of refined parameters	54	68	105	62	63	84
Robs	5.56	6.48	6.63	7.68	6.70	6.48
Rall	7.43	9.94	7.07	7.80	7.02	7.28
av. dist. (Å)	0.0064	0.0063	0.0079	0.0079	0.0097	0.0103
max. dist. (Å)	0.007	0.0077	0.0127	0.0113	0.0137	0.0132

Green and red backgrounds are related to kinematical and dynamical refinements, respectively. The data resolution limit in PETS2 was set to 1.4 Å^{-1} in all cases. Atomic displacement parameters (ADP) were refined as isotropic in all cases. The average (av. dist.) and maximal deviation (max. dist.) on atomic positions are given with respect to the bulk reference (ICSD 190347).

In continuous rotation, using a larger beam size gives a priori a better chance of keeping the particle in the beam throughout the tilt sequence. This also depends on the movement of the crystal when tilting the goniometer at a given rotation speed (eucentric quality of the goniometer). At IIT, with a configuration optimized for beam-sensitive material, the rotation speed is quite fast (2°/s) in order to limit the total acquisition time. With 0.5 s per frame exposure, the total acquisition time is 1 min for a rotation range of 120°. For this experimental setup, the use of a sample tracking system was found beneficial (see Materials and Methods). With a transmission electron microscope (TEM) usually utilized for analyzing larger crystals, finding one single TiO_2 nanorod in the 600 nm wide electron beam proved challenging but achievable. This issue can arise with some older-generation TEMs or even with recently marketed electron diffractometers, where using such a large electron beam (or selected area) is the only option to maintain parallel beam illumination. The dispersion of NPs on the TEM grid needs to be adapted to maximize the chance to find isolated particles. The key issue is ensuring that only one particle is within the beam throughout the entire rotation range, which may require several data sets to be acquired in order to obtain a few collected on one single TiO_2 nanorod. This is one disadvantage of using a large beam, but it does not in any way prevent a successful structural solution and refinement, as proved by the results indicated in Table . For kinematical refinement, the average deviation on atomic positions is below 0.02 Å with a maximal deviation of about 0.03 Å and Robs of 15%. This result, already quite good, is further improved in the dynamical refinement, where deviations in atomic positions are below 0.01 Å with an Robs value strongly reduced. The structural similarity with respect to the reference bulk brookite tells us that the NPs have essentially the same structure as the bulk (Figure).

2.

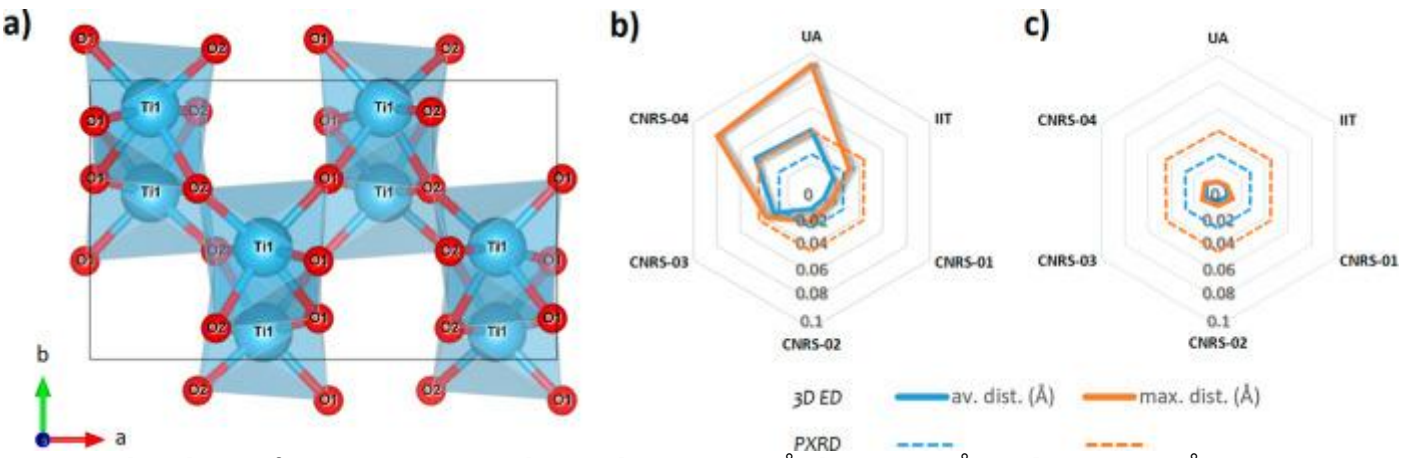

(a) TiO_2 brookite reference structure: *Pbca* with a = 9.174 Å, b = 5.449 Å, and c = 5.138 Å. (b,c) Radar plots showing the average (av. dist.) and maximal deviation (max. dist.) on atomic positions between the bulk reference and the structures obtained based on 3D ED data kinematical and dynamical refinements, respectively. In dashed lines are represented the deviations obtained for the PXRD kinematical refinement.

At UA, the reduction in beam size to 300 nm and a reduced rotation speed (0.4°/s) improve the applicability of 3D ED to capture the structure of a single TiO_2 nanorod. No particle tracking was applied during the continuous rotation, as the particle stays within the beam the whole tilt range. Only a few data sets were acquired, and these proved sufficient. The typical acquisition time was about 0.5 s per frame for a total acquisition time of about 3 min. As indicated in Table , it was possible to successfully solve the structure and perform both kinematic and dynamic

refinements with very good Robs values. Here, the deviations resulting from the kinematical refinement are a bit larger but can be strongly reduced using dynamical refinement and reach an accuracy equivalent to the previous case.

At CNRS, using a beam about 100 nm in size, the precession-assisted 3D ED data was acquired with a visual check at each tilt step to track the nanorod motion while acquiring the tilt series. In terms of total acquisition time, 15 min is a minimum for a 2° step-by-step acquisition of 3D ED data, including visual inspection of the NP position. Precession-assisted 3D ED data sets were acquired with different tilt steps and exposure times per frame to test how detrimental or beneficial the change of these parameters be. As indicated in Table , it was possible to successfully solve the structure and perform both kinematical and dynamical refinements with good Robs values for all data sets. The trend observed for data obtained with continuous rotation is broadly the same here, with just a greater maximum deviation in the case of the CNRS-04 data. Even in this case, the use of dynamic theory significantly increases the accuracy of the results. The structural similarity with respect to the reference bulk brookite is confirmed in all cases (Figure), also suggesting that using a tilt step of 2° is not detrimental in the present case.

This initial test on brookite demonstrates that the ab initio structure solution is feasible for relatively large NPs (typically ranging from 50 to 100 nm). This method can be applied using a wide range of instruments, with 3D ED data collected through either precession-assisted step-by-step or continuous rotation modes. It is, however, essential to ensure that the data collected are from a single individual of good crystalline quality. If this obvious prerequisite is met, then satisfactory results can already be obtained using kinematical approximation refinements with average deviations of atomic positions with respect to references less than 0.05 Å (Table and Figure). A certain disparity among the results is still observed with a maximal deviation of up to 0.08 Å. In terms of accurate structure analysis, this study shows once again that the use of full dynamic refinement brings additional benefits. Indeed, we notice a clear improvement in both reliability factors and atomic position accuracy with average and maximal deviations of about 0.01 Å for all data sets (Table and Figure). Such values are in perfect match with those obtained on larger crystals, as evidenced by the Round Robin on structure refinement quality with 3D ED performed recently.

Pushing the Lower Size Limit and Exploring Dynamical Effects in Crystals below 20 nm

In attempting to apply the above protocols to smaller NPs, namely, quasi-spherical particles below 20 nm, the experimental requirements appeared much more stringent. Particle tendency to aggregate, tiny beam requirement, absence of a proper particle position tracking system, and particle sensitivity to the beam reduce the options for collecting 3D ED data. While various tracking systems exist for instruments operating in either the TEM or STEM ,, mode, they may not be easily implemented in all experimental setups. Moreover, when using a small electron beam (below 30 nm in diameter, as in our ITO case; see below) to acquire 3D ED data on NPs smaller than 20 nm, the efficiency of these systems is severely challenged, highlighting the need for improved routines specifically adapted to small beams and NPs.

The need to reduce beam size may be the most restrictive requirement for some experimental TEM setups and may preclude any possibility of using 3D ED on such a tiny individual particle. As already mentioned for brookite, the primary concern is to prevent the contribution of multiple NPs during data collection. A second issue arises with the signal-to-noise ratio when a particle is supported by an amorphous membrane, usually composed of carbon. With a large beam, the contribution of the membrane becomes dominant, overshadowing the signal from the tiny crystal. Although not all reflections are equally impacted, the overall data quality can be compromised. Obtaining a parallel electron beam of suitable size, typically about twice the diameter of the particle, is possible on most modern TEMs equipped with an appropriate condenser lens system but is not feasible with all instrumental configurations. Although this adjustment is necessary to improve the signal-to-noise ratio, the use of a small, high-intensity beam may affect the particle stability depending on the nature of the NPs. Such conditions can result in a significant reduction in the available tilt range before crystal degradation occurs. To limit this effect, a small electron beam was formed under the lowest intensity conditions feasible with the JEOL F200 TEM (see Materials and Methods). An alternative method would be to operate the microscope in the STEM mode, which limits overall crystal illumination more effectively than the TEM mode. Subsequently, we encountered an additional challenge as the number of observed reflections often fell below ten times the number of refined parameters when maintaining the same data acquisition settings as for brookite. To address this issue, we used an exposure time of 4 s per frame to compensate for the reduction in NP size. Additionally, we utilized a cryogenic TEM holder, enabling data acquisition at −170 °C rather than at room temperature. With our instrumental setups and a 25 nm beam, an efficient track of a 10 nm particle position is not possible; consequently, continuous rotation 3D ED could not be used. For this study, we thus focus on precession-assisted step-by-step 3D ED data acquisition with a step of 2° (CNRS) to reduce the total acquisition time. In the case of brookite, we noticed that taking a step of 2° instead of 1° does not seem to have a detrimental effect on the results.

With this protocol, it is possible to acquire 3D ED data suitable for structure solution and refinements on quasi-spherical 10 nm ITO and ellipsoidal 15 nm anatase NPs (see Table , Figures and). As an initial observation, it is noteworthy to mention the high quality of the ED patterns obtained for these NPs, with an information limit extending beyond 2 $Å^{-1}$, as illustrated for ITO in Figure S4. From the structure refinements performed on 3D ED data sets for the two compounds under investigation here, we cannot notice a significant modification of their structure with respect to the bulk reference, as attested by the maximal deviation on atomic positions (maximum dist. in Table). It is worth mentioning that the results obtained from 3D ED kinematical refinements are already quite good, with deviations in atomic positions comparable with the ones obtained from synchrotron PXRD data. Dynamical refinements allow some improvement in the accuracy of atomic positions, adding the possibility to refine anisotropic ADP as done here (see the Crystallographic Information Files as Supporting Information). This is clear evidence that 3D ED can provide high-quality data, enabling access to the finer details of a structure for crystals approximately 10 nm in size.

2. Structure Refinement Results Obtained from Precession-Assisted 3D ED Data Recorded under Cryogenic Conditions Using a Precession Semi-Angle of 1.2°, a 2° Tilt Step, and a 4 s Exposure per Frame .

	ITO-01	ITO-02	ITO-03	anatase
Tilt Range (°)	[-35.7, +43]	[-43.7, +24.1]	*812 frames*	[-32.7, +43.3]
Cumul. Cover. *(sinθ/λ=0.8Å^{-1})*	100	99.8	100	100
Averaged Refl. All/Obs.	370/275	373/310	371/292	94/76
Redundancy	9.5	8.7	14.8	4.9
Rint (from PETS)	13.8	8.8	9.3	22.7
Number of refined parameters	8	8	9	4
Robs	7.91	6.1	7.77	10.92
Rall	10.59	7.91	10.22	12.35
max. dist. (Å)	0.0314	0.0189	0.0351	0.0291
Refl. All/Obs.	2529/1677	2386/1697		591/464
Number of parameters	52	48		43
Robs	6.43	4.71		3.59
Rall	8.54	6.25		4.18
max. dist. (Å)	0.0081	0.0086		0.0136

Exception is for ITO-03, recorded by serialED, consisting of ED frames recorded without precession with an exposure time of 0.5 s. Green and red backgrounds are related to kinematical and dynamical refinements, respectively. The maximal deviation (max. dist.) on atomic positions is given with respect to the bulk reference for ITO (ICSD 190347) and anatase (ICSD 9852).

3.

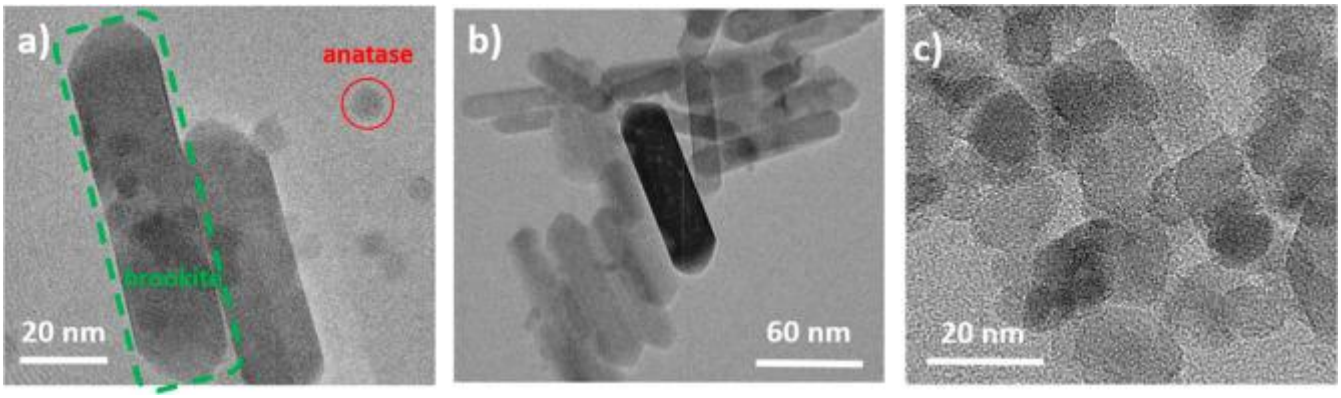

(a) Mix of brookite rods and anatase synthesized at 250° during 12 h at CNRS. (b) Pure brookite synthesized at 200° and 24 h at CNRS. (c) Pure anatase obtained from ICV-CSIC.

4.

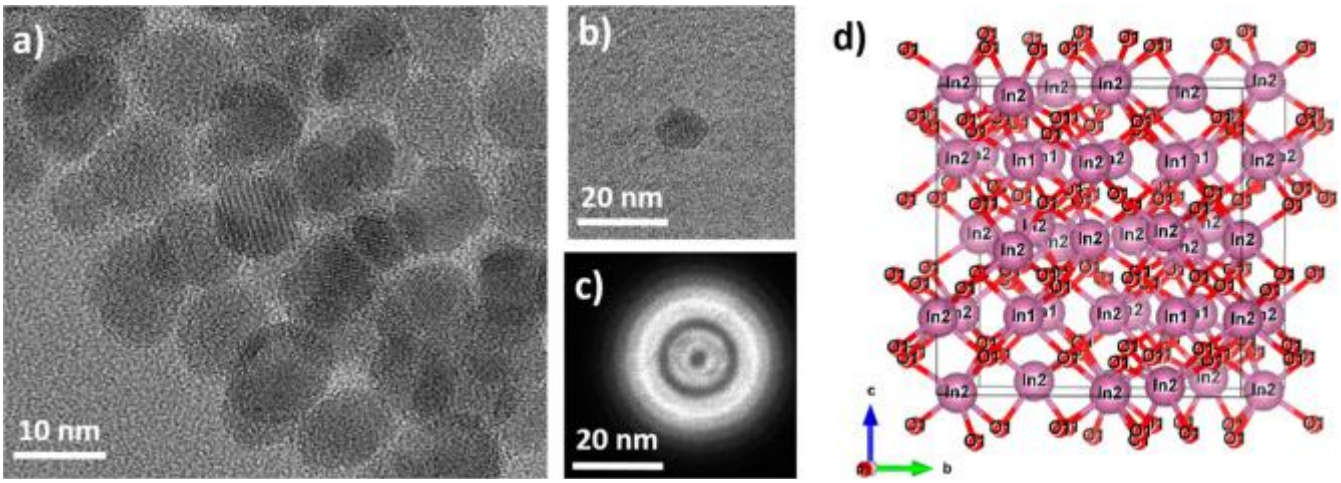

Open in a new tab

ITO NPs obtained from the group Functional Nanosystems at IIT (Genova□Italy). (a) NPs assembly showing the homogeneous particle size. (b) Isolated NPs suitable for 3D ED experiments. (c) Size of the electron beam used for the particle in (b). (d) ITO structure.

It is common to observe a significant decrease in the calculated *R*-values (Robs) when employing a dynamical refinement approach compared to kinematical refinement. This is what can be observed in the case of brookite (Table), with a value of Robs divided by 2 or more in all cases. This serves as a tangible indicator that the analysis of 3D ED data sets using full dynamical refinement was successful, allowing for a more comprehensive consideration of dynamical effects and, ultimately, achieving increased accuracy compared to kinematical refinement. However, upon examination of Table , only a small difference is found in the *R*-values obtained for the two refinement methods for ITO. One possible explanation for this result is that the size of the ITO NPs has been sufficiently reduced, making multiple scattering effects almost negligible. Additionally, the higher symmetry of ITO, in comparison to anatase, could play a role in the observed outcome by facilitating a more efficient averaging of reflection intensity during kinematical refinement due to increased redundancy (see Table). It is also important to note that there is a clear distinction between the data processing methods used for kinematical and dynamical refinements. Consequently, a direct comparison of the reliability factors is not feasible. For kinematical refinements, the average of symmetry-equivalent reflections is used, as it is assumed that symmetry-equivalent reflections have identical intensities regardless of where they were collected during the 3D ED tilt series. For dynamical refinements, this is not the case, as symmetrically equivalent reflections recorded in different frames of the 3D ED data have no reason to be identical, precisely because of multiple scattering events.

By working on symmetrically equivalent averaged reflections, *R*-values obtained by kinematical refinements are expected to be lower than for “non-averaged data”. Kinematical refinement on “non-averaged data” can be performed in JANA2020, leading indeed to a significant increase in the *R*-values, as illustrated in Table . The two refinements based on “non-averaged” data remain noncomparable, as a dynamical “frame-based non-averaged” refinement involves additional parameters compared to the kinematical approach (see Table), notably scaling factors for each frame of the 3D ED tilt series. In an effort to provide comparable numbers, Klar et al. recently proposed a method to perform kinematical “frame-based non-averaged” refinements using the same setup and parameters as for dynamical refinements. Such refinements can be performed in JANA2020 and were introduced to determine whether the

improvement from kinematical to dynamical refinements comes from a better description of dynamical effects or from differences in how the data are processed and refined. Kinematical "frame-based non-averaged" refinements mirror dynamical refinements in all aspects except that site occupancy for each atomic position are set to very low values. In the dynamic scattering theory framework, this reduction weakens the interaction between electrons and the crystal, making the intensities closer to the kinematical limit. The results (highlighted by a blue frame in Table) confirm a small but significant reduction of the Robs value (about 2–3%) for dynamical refinements compared to kinematical ones. This suggests that genuine dynamical scattering effects may still be present, even for such small ITO NPs, with dynamical refinements yielding enhanced accuracy in structure determination (Table).

3. Robs Values Obtained Depending on the Data Processing .

	averaged	non-averaged	frame-based non-averaged	frame-based non-averaged
ITO-01	**7.9**	10.1	8.5	**6.4**
ITO-02	**6.1**	8.3	7.3	**4.7**

a

"Averaged" is used to indicate that an averaging over symmetry-equivalent reflections is performed. "Non-averaged" when no such averaging is performed. Green and red backgrounds are related to kinematical and dynamical refinements, respectively. Values in bold are the values usually given for kinematical and dynamical refinements (see Table). Values given in blue frames correspond to values that should be the most comparable.

Strengths and Limitations of 3D ED

The aim of this paper is to demonstrate the ability of 3D ED to provide accurate information on the crystal structure when applied specifically to NPs. As a methodological study, this work relies on known structures to assess the strengths and limitations of the technique. For example, the NPs used previously all have structures very similar to those of their counterparts synthesized as larger crystals. This makes them ideal model systems for our study. Our results demonstrate that, when high-quality 3D ED data sets are acquired, detailed structural information can be obtained for NPs as small as 10 nm. In comparison with the Rietveld refinement of synchrotron PXRD data, the dynamical refinement of 3D ED data exhibits a more robust minimization process, reducing the likelihood of unphysical results while achieving comparable, if not superior, accuracy when compared to the related bulk structure. Notice that, in the case of ITO NPs, our synchrotron PXRD data failed to provide positively defined

anisotropic ADPs for the oxygen position, whereas 3D ED successfully did (see the CIF files in the Supporting Information). 3D ED as a single crystal diffraction technique has strengths in determining the crystal structure of NPs, in particular, accurate atomic positions and ADPs.

One limitation of 3D ED is to accurately detect small lattice parameter variations, such as those resulting from surface relaxation in NPs or slight changes in doping element concentration. Inaccuracies in 3D ED unit cell parameters result primarily from distortions in the electron microscope optics, causing imprecision of up to several percent in cell lengths and up to half a degree in angles. This reduces the accuracy compared to SCXRD and PXRD. However, distortions can be corrected during data reduction and were systematically addressed in this study. This correction improves the estimation of lattice parameters and enables reliable conclusions regarding their relative values. Nonetheless, distortion correction does not compensate for inaccuracies in the absolute scale of the lattice parameters, which arise from the inherent difficulty in precisely determining the apparent detector-to-specimen distance. This second source of error can be overcome by using an internal standard during data collection. In this study, 3D ED data were not simultaneously collected on an internal standard. As a result, achieving absolute accuracy better than 1% is difficult, which is generally insufficient for drawing reliable conclusions about the potential differences between NPs and bulk materials. Note that if both distortions and calibration issues are properly addressed, the imprecision in lattice parameters may be reduced to less than 0.5%, allowing access to small lattice parameter evolution at the nanoscale, as shown in a recent study on oxide thin films.

As nonresonant XRD, 3D ED also has limitations in estimating low dopant concentrations or in determining the ratio of mixed occupancy sites for elements with similar atomic numbers, such as In and Sn in ITO. For ITO, structure refinements, including dynamical refinements, do not provide any indication of the Sn content present in the material. To showcase the capabilities of 3D ED in determining mixed occupancy ratios in NPs, we turn to pseudobrookite $MgTi_2O_5$, which offers a greater contrast between chemical species occupying the same atomic sites than ITO. $MgTi_2O_5$ crystallizes in an orthorhombic unit cell and a *Bbmm* space group. All cations occupy two nonequivalent, highly deformed octahedral sites, M1 and M2, with M1 being larger and more deformed than M2 (see Figure). Larger Mg^{2+} ions preferentially occupy the more distorted M1 sites, while smaller Ti^{4+} ions favor the less distorted M2 sites. The challenge with this compound is that the occupancy of these two sites can vary, depending on its thermal history. In a study by Yang and Hazen, different $MgTi_2O_5$ samples were synthesized at temperatures between 600 and 1400 °C using the flux method to produce single crystals suitable for SCXRD analyses. These analyses provide insight into the occupancy of the M1 and M2 sites, indicating that samples synthesized at lower temperatures exhibit a strong preference for M1 site occupancy, which is almost exclusively occupied by Mg, leading to a more cationic ordered state. As the synthesis temperature increases, cationic disorder becomes more pronounced, with the M1 site in the sample synthesized at 1400 °C being half occupied by Ti. To test whether 3D ED can provide such “detailed” structural information, a 3D ED data set was collected at CNRS on a $MgTi_2O_5$ NP about 30 nm in size using an electron beam diameter of 65 nm. Given the significant differences in synthesis conditions and crystal sizes from the study by Yang and Hazen, the Mg/Ti ratios at the M1 and M2 sites in the NPs remain a priori unknown.

5.

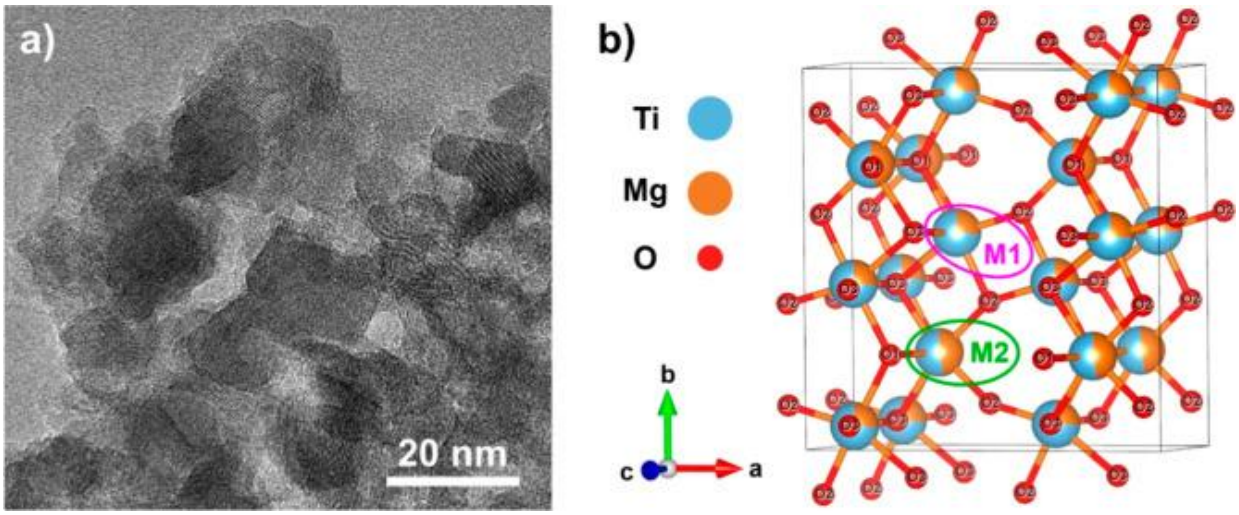

Open in a new tab

(a) Assembly of $MgTi_2O_5$ NPs with heterogeneous particle size. (b) $MgTi_2O_5$ structure from the 3D ED study (this work), showing mixed Mg/Ti occupancy at cationic sites M1 and M2.

Two scenarios were tested for both kinematical and dynamical refinement: one in which Ti and Mg were randomly distributed, with 1/3 Mg occupancy at both M1 and M2 sites, and another in which the distribution of Mg and Ti at these sites was refined while maintaining the overall $MgTi_2O_5$ composition. The summary of the results in Table highlights a key observation: the structural parameters, including the Mg/Ti distribution, obtained from both kinematical and dynamical refinements are largely identical within error margins. Interestingly, the reliability factors obtained from the kinematical refinement are quite low (around 10%), suggesting that the reduction in crystal size weakens dynamical effects, leading to improved modeling of diffracted intensities within the kinematic approximation. However, as in previous cases, an improvement in reliability factors is still observed when applying the dynamical theory in the refinement. Interestingly, while the difference in reliability factors between a random distribution (see Table S2) and a preferred localization of cations onto M1 or M2 sites is minimal for the kinematical refinement (Robs goes from 10.92 to 10.74), the dynamical refinement clearly distinguishes between both scenarios (Robs goes from 7.74 to 6.86). Finally, the results indicate that the NP synthesis route leads to a $MgTi_2O_5$ compound with a strong cationic disorder, more pronounced than that observed for the crystals synthesized at 1400 °C. This is accompanied by a change in the mean M–O distances, with a decrease for M1–O and an increase for M2–O, consistent with the SCXRD study.

4. Structural Parameters Obtained by 3D ED for a 30 nm $MgTi_2O_5$ NP .

Space Group: *Bbmm*(63), a = 9.7974(72) Å, b = 9.9943(71) Å, c = 3.7640(16) Å					
R(obs)=10.74, R(all)=11.24 , wR(all)=27.14, GoF(obs)=2.88 measured / observed [I>3σ(I)] reflections = 213 / 199, 15 refined parameters					
R(obs)=6.86, R(all)=8.06 , wR(all)=14.75, GoF(obs)=3.21 measured / observed [I>3σ(I)] reflections = 1393 / 968, 51 refined parameters g_{max} (Å^{-1}) =1.6, Sg_{max} (Å^{-1}) =0.01, RSg_{max}=0.75 steps = 256					
Atom	**x**	**y**	**z**	**Occupancy**	**U (Å^2)**
M1 $Ti_1 : Mg_1$	0.8091(4)	0.25	0	0.54(2) : 0.46(2)	0.0062(13)
	0.8104(2)	0.25	0	0.529(8) : 0.471(8)	0.0058(4)
M2 $Ti_2 : Mg_2$	0.1372(3)	0.4364(2)	0	0.730(12) : 0.270(12)	0.0072(10)
	0. 13750(13)	0.43632(13)	0	0.735(4) : 0.265(4)	0.0081(3)
O_1	0.2372(9)	0.25	0	1.0	0.0102(16)
	0.2393(4)	0.25	0	1.0	0.0120(7)
O_2	0.0478(7)	0.8839(7)	0	1.0	0.0153(14)
	0.0479(3)	0.8833(3)	0	1.0	0.0149(6)
O_3	0.3101(6)	0.9284(5)	0	1.0	0.0087(13)
	0.3100(3)	0.9285(3)	0	1.0	0.0126(5)

a

Green and red backgrounds are related to kinematical and dynamical refinements, respectively.

Capturing the Structure of NPs in Motion

Working under cryogenic conditions reduces electron beam damage to NPs and improves the quality of the 3D ED data obtained. During these experiments, it was observed that the electron beam-induced NP movements were likely caused by changes in the amorphous layer formed during the sample freezing and present all over the carbon support film. As the beam reached a particle and its surroundings, the amorphous layer sublimated and bubbles were observed (see Figure). When these bubbles reach a particle, a movement is induced in the form of a rotation. This induced rotation of the NP can actually be exploited by collecting diffraction data while the NP is in motion. It is thus possible to collect a tilt series over a small angular range, with the direction and angle of tilt being random and unknown. Nevertheless, in this way, by collecting small tilt series over many randomly oriented NPs, it should be possible to access the entire reciprocal lattice. This data collection strategy can be related to serial electron crystallography (serialED), which is used for highly beam-sensitive materials, where typically a single diffraction pattern is collected per crystal. −

6.

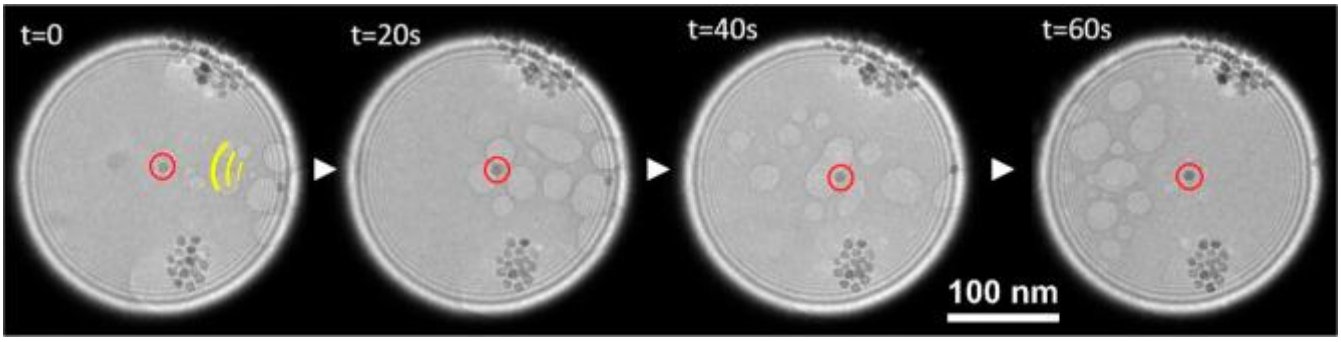

Open in a new tab

Sequential images showing the propagation of a bubble wavefront (emphasized in yellow at t = 0) from the right to the left of the images passing through an isolated NP encircled in red. Upon impact, this wavefront induces a motion of the NPs with a rotational component. The average diameter of NPs is 10 nm. This rotation is best seen in the movie given as Supporting Information by observing change in the contrast of the particles (diffraction contrast).

The diffraction pattern analysis is done by generating a large set of simulated ED patterns (templates ,) that we compare with the experimental patterns in order to find their orientation. Only the cell parameters and the Laue class should be known, as the indexing is based on the position of the diffracted spots regardless of their intensities. Cell parameters can be obtained either by exploiting conventional 3D ED data collected over a small angular range (usually not suitable for structure solution but usable for lattice parameter determination) or by other sources such as PXRD. Once the experimental patterns have been indexed, the data analysis can proceed as for a conventional 3D ED data set. Sections of the reciprocal space and extinction conditions can be examined, giving further insight into the symmetry elements and possible space groups. This data collection strategy was applied to ITO NPs in motion, capturing more than 800 ED frames (without precession) from dozens of NPs. The data analysis was conducted using the serialED options provided by the PETS 2.0 program, as detailed in its user manual (available at pets.fzu.cz). Data completeness reached 100% (for sin θ/λ = 0.8 $Å^{-1}$) with a redundancy of about 15. Note that, although the information was truncated for structure refinement, the information limit extends beyond 2.25 $Å^{-1}$ (see Figure S4). Based on kinematical refinements, it was possible to obtain good R-values (see Table) with a maximal deviation of 0.03 Å with respect to the reference bulk structure. The accuracy of atomic positions is thus comparable to the results obtained from kinematical refinements of precession-assisted 3D ED data, confirming that averaging a large number of randomly oriented ED patterns can produce quality 3D ED data sets suitable for structure analyses. Note that, with such data, it is still not possible to perform dynamical refinements that, notably, require an optimization of both sample thickness and frame orientation. Even if the average thickness of the NPs is known and identical, frame orientation optimization failed and prevented convergence of the refinement.

Conclusions

This account explores some of the challenges involved in acquiring 3D ED data for NPs. Each phase of the experiment is examined, encompassing sample preparation, instrument characteristics, and recommendations for the most appropriate experimental 3D ED approach. Our aim is not merely to provide a proof-of-concept for structure solution but to present a groundbreaking achievement, i.e., the ability to obtain accurate structure refinements from a single NP down to 10 nm in size. This remarkable feat unveils two significant findings. First, we observe the persistence of dynamical scattering effects, albeit reduced, even at the nanoscale of 10 nm. This challenges conventional wisdom and demonstrates once again that if reliable, accurate structure refinements are the goal, then dynamic effects must be taken into account. If this is done, then the results obtained are excellent, whatever the data set, and, in any case, equal to or better than what can be obtained by PXRD. Second, our study still reveals that it would be an exaggeration to say that performing refinements in the frame of the kinematical approximation leads to erroneous structures. We show here that the accuracy can be quite good and, for some cases, at the level of what can be obtained with PXRD. Nevertheless, and this remains the major difference, accuracy appears to be data set-dependent, with no clear correlation with reliability factors.

The recommendations outlined in this paper are based on a series of experiments carried out on different samples and on different instrumental configurations. Observations from implementing these guidelines support the ability of 3D ED data to achieve remarkably accurate refinements, even for tiny crystals. Although this report attests that it is possible to acquire 3D ED data on isolated crystals 10 nm in diameter, this is not an absolute limit. This limit must be able to be pushed toward smaller NPs by better optimization of data collection and tracking the NP position during the data collection. Beyond merely questioning the crystal size limits that 3D ED can achieve, we show here that most TEM setups should be able to analyze crystals in the 100–50 nm range, even when using a somewhat wide beam (diameter around 600 nm). This latter case corresponds to what is currently available on dedicated electron diffractometers (with a still slightly wider beam). The main challenge lies in isolating a single particle from a beam significantly wider than the particle itself, but this task is achievable. If we now aim to extend the use of 3D ED to study nanodomains (for instance, in thin films, ceramics, or geological materials), it is clear that to collect 3D ED data from a 10 nm domain embedded in a matrix, working with an electron nanobeam close to that size is essentially necessary. This consideration should be taken into account when selecting an experimental configuration to use 3D ED in the field of nanotechnology and materials science.

Dynamical scattering effects in ED should no longer be seen as a difficulty or even an obstacle but as an opportunity to explore the crystalline structure of nano-objects. There is little doubt that the potential of 3D ED will increasingly be exploited for studying smaller and smaller crystals and/or domains. This study holds promise: to provide access to precise and reliable structural information (such as site occupancy or atomic displacement parameters) that cannot be obtained as easily through other approaches.

Materials and Methods

Synthesis

Titanium dioxide (TiO_2) NPs are used in a wide range of applications and exist in three main phases: anatase, brookite, and rutile. As a bulk material, rutile is the stable phase, whereas brookite and anatase are metastable and easily transformed to rutile when heated. However, when grain size is small enough, the phase relationships and transition kinetics may be dramatically modified. This is because the phase stability depends upon surface energy differences among the three phases. With grain size below 14 nm, anatase is more stable than rutile. Anatase is also more stable than brookite for NPs with a size smaller than 11 nm, which suggests that a phase transition from brookite to anatase also may take place. Given the above considerations, obtaining TiO_2 in the form of NPs combining both a controlled particle size and a single polymorph is not trivial, as illustrated in Figure a.

Brookite was synthesized using a hydrothermal approach. In a Teflon cup, placed within a stainless steel autoclave (Berghof, DAB-3), 0.8 mL of titanium(IV) bis (ammonium lactato) dihydroxide (TALH, Sigma-Aldrich) was combined with 7 M urea (Sigma-Aldrich) to achieve a final volume of 8 mL. The Teflon cup was sealed within the autoclave and subjected to a temperature of 200 °C for 24 h using an electric furnace. After the reaction, the Teflon cup was cooled to room temperature, and the resulting product was washed with ethanol and centrifuged to isolate the purified residue. This final product was subsequently dried at 60 °C in an oven. Under these conditions, brookite NPs were obtained in the form of nanorods of approximately 70 nm in length and a width of around 30 nm (Figure b). These nanorods are here used as a reference for "large size" NPs that would allow us to test different data acquisition protocols. Brookite structure□SG: *Pbca* (61) with a = 9.1740(2) Å, b = 5.4490(2) Å, and c = 5.1380(2) Å (ICSD 36408)□is also interesting as a model system since, despite having only 3 atomic positions (1 Ti and 2 O), all 3 atomic coordinates (9 parameters) are free and can be refined.

Anatase NPs of approximately 15 nm in diameter (Figure c) were synthesized through a one-step semisolvothermal route using titanium(IV) tetrabutoxide ($Ti(OBut)_4$, Fluka, 98%) and trifluoroacetic acid (CF_3COOH, Aldrich, 70%, TFAA). In a typical procedure, 5 mL of $Ti(OBut)_4$ is introduced in a 50 mL Teflon-lined stainless-steel autoclave, together with 1.9 g of TFAA. A small amount of deionized water (0.4 mL) is added to accelerate the hydrolysis reaction. The system is then heated at 200 °C for 24 h. The obtained white-brown precipitate is washed several times with butanol, ethanol (96%), and water and then dried at 80 °C. Finally, an additional heat treatment is carried out at 200 °C for 2 h to clean the surface. In anatase structure□SG: $I4_1/amd$ (141) with a = 3.7842(13) Å and c = 9.5146(15) Å (ICSD 9852)□only 2 atomic positions (1 Ti and 1 O) are present with only one atomic coordinate to refine.

ITO NPs of approximately 10 nm (Figure) were synthesized using a multistep procedure. As the first step, a 500 mL three-neck round flask was filled with 208 mL of oleyl alcohol (Sigma-Aldrich, 85% purity) and left at 150 °C to degas for 3 h under a flux of nitrogen. Indium(III) and tin(IV) acetate (Sigma-Aldrich) were added, along with 32 mL of oleic acid (Sigma-Aldrich, 90% purity), to a 100 mL three-neck round-bottom flask. Under stirring, the flask content was degassed for 3 h under a nitrogen flux, allowing tin and indium oleates to form. After degassing, the flask with oleyl alcohol, which will act as the reaction vessel, was kept under a flux of 0.130 L/min of nitrogen and heated to 290 °C. Indium and tin precursors were transferred to a syringe and injected in the hot oleyl alcohol using a syringe pump at an injection rate of 4.8 mL/min. NPs with an average diameter of 10 nm and a 10.8% doping level (Sn/tot) were obtained 15 min after the injection ended. The solution was then centrifuged at 5540*g* for 10 min, using ethanol as an antisolvent. The supernatant was discarded, the material was

dispersed in hexane, ethanol was added, and the solution was centrifuged again by using the same parameters. Finally, the NPs were stored in octane. In the ITO structure□SG: *Ia* $\bar{3}$ (206) with a = 10.12690(1) Å (ICSD 190347)□3 atomic positions (2 In and 1 O) are present with one atomic coordinate to refine for one indium position and the 3 atomic coordinates for the oxygen position.

$MgTi_2O_5$ was synthesized using a hydrothermal method. The first step involved preparing an aqueous urea solution by dissolving 12 g of urea in 30 mL of distilled water, resulting in a solution with a concentration of approximately 6.66 mol L^{-1}. In this solution, 3.84 g of magnesium nitrate(II) hexahydrate was dissolved. Simultaneously, a second solution was prepared by mixing 40 mL of ethylene glycol with 6 mL of titanium isopropoxide in a 250 mL flask. Both solutions were then combined under constant stirring at 90 °C for 24 h. The resulting product was recovered, washed with distilled water, and dried in an oven at 60 °C. Finally, the product was calcined at 600 °C for 2 h, yielding $MgTi_2O_5$ NPs with heterogeneous sizes, around 30 nm. In $MgTi_2O_5$ structure□SG: *Bbmm* (206) with a = 9.9789(4) Å and b = 9.9789(4) Å and c = 3.7478(3) Å (ICSD 51022)□5 atomic positions (2 mixed Mg/Ti and 3 O) are present with 3 atomic coordinates to refine for the mixed Mg/Ti positions and 5 atomic coordinates for the oxygen positions. The Mg/Ti ratios at cation sites M1 and M2 (Figure) are a priori unknown and need to be refined.

TEM Grid Preparation

Single-crystal 3D ED requires isolated particles from which diffraction patterns can be taken without interference from differently oriented particles caught within the beam. Thus, particle agglomerations (Figures and) pose a significant challenge during data acquisition, as nearby particles would interfere with the analysis during sample rotation. Ideally, isolated NPs (Figure b) need to be found on the TEM grid for 3D ED experiments. For instrumental configurations where the formation of small parallel illumination beams is not possible, the agglomeration of NPs could constitute a serious problem preventing any analysis.

In this study, we addressed this issue by employing an ultrasonic bath (typically for 30 min) and using ethanol as a solvent for particle dispersion. Depending on the materials, dispersion may vary in difficulty, and alternative solvents may need to be explored for optimal results. Once dispersed in an appropriate solvent, a drop of the solution containing the NPs was deposited on 3 mm diameter TEM grids coated with holey-carbon films. For grids prepared in air, drying could be accelerated by using infrared light. If contamination appeared rapidly around the NPs being analyzed, then the use of an ion cleaner (several minutes with a JEOL EC-52000IC) before inserting the grid into the TEM can circumvent this problem. Alternatively, it is also possible to use a plasma cleaner with a much shorter time.

Instruments

A few points related to instrumentation are important for the optimal 3D ED data collection of NPs when aiming for the best structure refinement. The instrumental features to consider are parallel beam illumination, appropriate probe size, quality of the goniometer stage, possibility to track the crystal position while tilting the stage, and detector quality.

When small, high-intensity electron beams are required to accommodate the size reduction of NPs, fast 3D ED data collection strategies can help to minimize potential beam-induced degradation. However, the challenge lies in tracking the movements of a small NP in continuous rotation 3D ED working with a small beam size (typically below 100 nm).

When the diffracting volume is greatly reduced, much lower diffracted intensities are expected, even when working with an appropriate high-intensity probe size. In this case, hybrid pixel detectors can be a real asset for studying the size limit of NPs by 3D ED. In this work, only instrumental configurations with hybrid pixel detectors are considered.

Keeping the above comments in mind, we test different data collection strategies in order to propose the most appropriate one depending on the size of the particle, but also taking into account the goal, i.e., structure solution only or accurate structure refinement. With regard to this last point, we have also collected PXRD data on all our samples, which will provide a basis for comparison with the results obtained by 3D ED.

The JEOL F200 TEM at CNRS is working at 200 kV (FEG source) and equipped with an ASI CheeTah Medipix3 hybrid-pixel detector. It was used for most of the results obtained in the present study. In this case, precession-assisted 3D ED acquisition was used, with the precession motion generated by a NanoMEGAS Digistar unit (the precession angle was in the range of 1.2° to 1.4° see tables to access the information for each recorded data set). 3D ED data were all acquired in the TEM probe mode using the Instamatic interface. The 4-stage probe-forming optical system independently controls the intensity and the convergence angle of the electron beam. Thanks to this and using a condenser aperture of 10 μm, it is possible to form a quasi-parallel nanobeam of about 10 nm or even less with a convergence angle below 1 mrad. For a configuration with a beam diameter of about 100 nm (used for TiO_2 brookite), the electron flux density is estimated at 24 $e^- Å^{-2} s^{-1}$. In contrast, for a 25 nm wide beam (used for ITO), the flux density increases to approximately 380 $e^- Å^{-2} s^{-1}$. For a stepwise precession-assisted 3D ED experiment using a small beam, the fluence on the sample is very high, reaching more than tens of thousands of $e^- Å^{-2}$. Where indicated in the text, we use a GATAN Elsa cryo-transfer holder but cool it only once in the TEM.

FEI TECNAI G2 F20 X-TWIN TEM @ UA is working at 200 kV (FEG source) and equipped with an ASI CheeTah Timepix3 hybrid-pixel detector. In this case, the 3D ED acquisitions were performed in continuous rotation. Using a condenser aperture of 20 μm, it is possible to form a parallel nanobeam of approximately 200–300 nm in diameter and use it to perform continuous rotation 3D ED experiments. For this configuration, the electron flux density is estimated at 0.66 $e^- Å^{-2} s^{-1}$, corresponding for TiO_2 brookite to a fluence of 130 $e^- Å^{-2}$.

The ZEISS LIBRA 120 TEM @ IIT is working at 120 kV (LaB6 source), equipped with an ASI Timepix1 hybrid-pixel detector. Using a condenser aperture of 20 μm, it is possible to form a parallel nanobeam of approximately 600 nm in diameter and use it to perform continuous rotation 3D ED experiments with a tracking system. For this configuration, the electron flux density is 0.1 $e^- Å^{-2} s^{-1}$, corresponding for TiO_2 brookite to a fluence of 6 $e^- Å^{-2}$. The crystal tracking software for the Zeiss Libra ensures the crystal sample remains consistently illuminated during experiments by adjusting the microscope's lenses. It works similarly to Fast-ADT and depends on the stable and precise movement of the microscope's goniometer to track

the crystal accurately. First, the software records a reference path by rotating the crystal within a user-defined range and mapping its movements. Once this path is set, the diffraction settings are applied, and the electron beam is adjusted in real time to stay aligned with the crystal's movement. This automatic correction for any shifts or stage movements ensures that the crystal stays within the illuminated area throughout the experiment.

MCX Beamline @ Elettra synchrotron PXRD patterns were collected using transmission geometry with powdered samples contained in a capillary. Structure analysis through Rietveld refinement of PXRD patterns provides a robust counterpoint to the results obtained by 3D ED, representing the conventional approach for diffraction-based analysis of such materials. Rietveld refinement was conducted using the FullProf software package, while graphic representations were generated using WinPlotr and VESTA. To ensure better alignment with single-crystal data procedures (integration and least-squares refinement), powder diffraction analysis was performed in two steps. The first step involved Le Bail refinement, optimizing only the profile and background parameters. In the second step, the previously optimized parameters were fixed, and Rietveld refinement was carried out. Anisotropic displacement parameters were refined for each atom, except for the oxygen site in the ITO sample, where the refinement converged toward unphysical values. Anisotropic size broadening has been treated by a general phenomenological model, using the Scherrer formula, that considers the size broadening can be written as a linear combination of spherical harmonics. Finally, the instrumental resolution function was evaluated experimentally with the use of a Si powder standard. A summary of the PXRD results is provided in Table S1, and the PXRD profiles are presented in Figures S1–S3 for brookite, anatase, and ITO, respectively.

3D ED Data Reduction and Analysis

The handling of the 3D ED data involves two distinct phases. First, the data reduction phase, which focuses on analyzing the raw data, consists of a series of diffraction patterns recorded at various tilt angles. For this, the software PETS2 has been used. Its purpose is to identify reflections within the frame series and reconstruct the reciprocal space in 3D. The data processing procedure provides unit cell parameters, reflection indexing, and integrated diffracted intensities corresponding to the *hkl* indices.

Second, the actual structure analysis phase involves deriving a structural model from these intensities ab initio, followed by a refinement through comparison of calculated intensities from the model with experimental ones. For the structure solution, based on a kinematical approximation, the software Superflip, utilizing the charge-flipping algorithm, was employed.

For structure refinement, two strategies were employed: either assuming kinematical approximation (kinematical refinement) or accounting for dynamical scattering effects (dynamical refinement). Dynamical refinement offers a more precise modeling of the ED process and, currently, can only be performed using the software Jana2020 and its Bloch-wave calculation module Dyngo. Jana2020, which also includes Superflip, can conduct both kinematical and dynamical refinements for precession-assisted 3D ED and continuous rotation

3D ED data. The observed reflections are those above 3 sigma, and refinements are carried out on F^2.

Supplementary Material

nn5c01764_si_001.pdf (1.2MB, pdf)
nn5c01764_si_002.zip (2.8MB, zip)
Download video file (8.5MB, mp4)

Glossary

Abbreviations

3D
three-dimensional

ED
electron diffraction

PEDT
precession-assisted electron diffraction tomography

cRED
continuous rotation electron diffraction

TEM
transmission electron microscope

PXRD
powder X-ray diffraction

SCXRD
single-crystal X-ray diffraction

NPs
nanoparticles

ITO
indium tin oxide

ADP
atomic displacement parameters.

3D ED and XRPD data are available at https://zenodo.org/communities/naned the NanED□Electron nanocrystallography project repository hosted by Zenodo.

The Supporting Information is available free of charge at https://pubs.acs.org/doi/10.1021/acsnano.5c01764.

- Rietveld refinement from synchrotron data, example of diffraction patterns, structure refinement results, and structural parameters (PDF)
- crystallographic information files resulting from the structure refinements conducted in this work (ZIP)
- Rotation of NPs being impacted by a bubbles wavefront (MP4)

E.C.O., S.G., M.D.F.D., P.B., J.H., and M.G. performed electron diffraction experiments. E.C.O., S.G., M.D.F.D., P.B., J.H., M.G., and L.P. analyzed electron diffraction data. E.C.O., L.R., E.B., V.P., I.K., and A.C.-A. performed NP synthesis. E.C.O. and J.P. performed powder X-ray diffraction experiments. C.P. analyzed powder X-ray diffraction data. E.C.O. and P.B. wrote the manuscript with contributions from all authors.

This research was supported by the European Union's Horizon 2020 research and innovation program under the Marie Skłodowska-Curie grant agreement No. 956099 (NanED□Electron Nanocrystallography□H2020-MSCA-ITN). J.H. and S.G. acknowledge the financial support of the Research Foundation Flanders (FWO, Belgium) project SBO S000121N. A.C.-A acknowledges the grant FPU21/03335 funded by MICIU/AEI/10.13039/501100011033 and by

the FSE+, and the project TED2021-132779B-I00 funded by MICIU/AEI/10.13039/501100011033 and by the European Union NextGenerationEU/PRTR. I.K. and L.R. acknowledge the financial support of the European Union's Horizon 2020 European Research Council under grant agreement no. 850875 (Light-DYNAMO project).
The authors declare no competing financial interest.

References

1. Lah, N. A. C. ; Zubir, M. N. M. ; Samykano, M. A. . Engineered Nanomaterial in Electronics and Electrical Industries. In Handbook of Nanomaterials for Industrial Applications; Elsevier, 2018; pp 324–364. [Google Scholar]

2. Ndolomingo M. J., Bingwa N., Meijboom R.. Review of Supported Metal Nanoparticles: Synthesis Methodologies, Advantages and Application as Catalysts. J. Mater. Sci. 2020;55(15):6195–6241. doi: 10.1007/s10853-020-04415-x. [DOI] [Google Scholar]

3. Ba Z., Han Y., Qiao D., Feng D., Huang G.. Composite Nanoparticles Based on Hydrotalcite as High Performance Lubricant Additives. Ind. Eng. Chem. Res. 2018;57:15225–15233. doi: 10.1021/acs.iecr.8b02831. [DOI] [Google Scholar]

4. Patra J. K., Das G., Fraceto L. F., Campos E. V. R., Rodriguez-Torres M. D. P., Acosta-Torres L. S., Diaz-Torres L. A., Grillo R., Swamy M. K., Sharma S., Habtemariam S., Shin H.-S.. Nano Based Drug Delivery Systems: Recent Developments and Future Prospects. J. Nanobiotechnol. 2018;16(1):71. doi: 10.1186/s12951-018-0392-8. [DOI] [PMC free article] [PubMed] [Google Scholar]

5. Wong K., Dia S.. Nanotechnology in Batteries. J. Energy Resour. Technol. 2017;139(1):014001. doi: 10.1115/1.4034860. [DOI] [Google Scholar]

6. Savage N., Diallo M. S.. Nanomaterials and Water Purification: Opportunities and Challenges. J. Nanoparticle Res. 2005;7(4–5):331–342. doi: 10.1007/s11051-005-7523-5. [DOI] [Google Scholar]

7. Toso S., Imran M., Mugnaioli E., Moliterni A., Caliandro R., Schrenker N. J., Pianetti A., Zito J., Zaccaria F., Wu Y., Gemmi M., Giannini C., Brovelli S., Infante I., Bals S., Manna L.. Halide Perovskites as Disposable Epitaxial Templates for the Phase-Selective Synthesis of Lead Sulfochloride Nanocrystals. Nat. Commun. 2022;13(1):3976. doi: 10.1038/s41467-022-31699-1. [DOI] [PMC free article] [PubMed] [Google Scholar]

8. Cowley, J. M. Diffraction Physics, 3rd rev. ed.; North-Holland Personal Library; Elsevier: New York, 1995. [Google Scholar]

9. Gemmi M., Mugnaioli E., Gorelik T. E., Kolb U., Palatinus L., Boullay P., Hovmöller S., Abrahams J. P.. 3D Electron Diffraction: The Nanocrystallography Revolution. ACS Cent. Sci. 2019;5(8):1315–1329. doi: 10.1021/acscentsci.9b00394. [DOI] [PMC free article] [PubMed] [Google Scholar]

10. Kolb U., Gorelik T., Kübel C., Otten M. T., Hubert D.. Towards Automated Diffraction Tomography: Part I□Data Acquisition. Ultramicroscopy. 2007;107(6–7):507–513. doi: 10.1016/j.ultramic.2006.10.007. [DOI] [PubMed] [Google Scholar]

11. Mugnaioli E., Gorelik T., Kolb U.. Ab Initio Structure Solution from Electron Diffraction Data Obtained by a Combination of Automated Diffraction Tomography and Precession Technique. Ultramicroscopy. 2009;109(6):758–765. doi: 10.1016/j.ultramic.2009.01.011. [DOI] [PubMed] [Google Scholar]

12. Nederlof I., Van Genderen E., Li Y.-W., Abrahams J. P.. A Medipix Quantum Area Detector Allows Rotation Electron Diffraction Data Collection from Submicrometre Three-Dimensional Protein Crystals. Acta Crystallogr., Sect. D:Biol. Crystallogr. 2013;69(7):1223–1230. doi: 10.1107/S0907444913009700. [DOI] [PMC free article] [PubMed] [Google Scholar]

13. Palatinus L., Petříček V., Corrêa C. A.. Structure Refinement Using Precession Electron Diffraction Tomography and Dynamical Diffraction: Theory and Implementation. Acta Crystallogr., Sect. A:Found. Adv. 2015;71(2):235–244. doi: 10.1107/S2053273315001266. [DOI] [PubMed] [Google Scholar]

14. Palatinus L., Corrêa C. A., Steciuk G., Jacob D., Roussel P., Boullay P., Klementová M., Gemmi M., Kopeček J., Domeneghetti M. C., Cámara F., Petříček V.. Structure Refinement Using Precession Electron Diffraction Tomography and Dynamical Diffraction: Tests on Experimental Data. Acta Crystallogr., Sect. B:Struct. Sci., Cryst. Eng. Mater. 2015;71(6):740–751. doi: 10.1107/S2052520615017023. [DOI] [PubMed] [Google Scholar]

15. Nannenga B. L., Shi D., Leslie A. G. W., Gonen T.. High-Resolution Structure Determination by Continuous-Rotation Data Collection in MicroED. Nat. Methods. 2014;11(9):927–930. doi: 10.1038/nmeth.3043. [DOI] [PMC free article] [PubMed] [Google Scholar]

16. Birkel C. S., Mugnaioli E., Gorelik T., Kolb U., Panthöfer M., Tremel W.. Solution Synthesis of a New Thermoelectric Zn 1+ x Sb Nanophase and Its Structure Determination Using Automated Electron Diffraction Tomography. J. Am. Chem. Soc. 2010;132(28):9881–9889. doi: 10.1021/ja1035122. [DOI] [PubMed] [Google Scholar]

17. Feyand M., Mugnaioli E., Vermoortele F., Bueken B., Dieterich J. M., Reimer T., Kolb U., de Vos D., Stock N.. Automated Diffraction Tomography for the Structure Elucidation of Twinned, Sub-micrometer Crystals of a Highly Porous, Catalytically Active Bismuth Metal–Organic Framework. Angew. Chem., Int. Ed. 2012;51:10373. doi: 10.1002/anie.201204963. [DOI] [PubMed] [Google Scholar]

18. Mugnaioli E., Andrusenko I., Schüler T., Loges N., Dinnebier R. E., Panthöfer M., Tremel W., Kolb U.. Ab Initio Structure Determination of Vaterite by Automated Electron Diffraction. Angew. Chem., Int. Ed. 2012;51(28):7041–7045. doi: 10.1002/anie.201200845. [DOI] [PubMed] [Google Scholar]

19. Bhat S., Wiehl L., Molina-Luna L., Mugnaioli E., Lauterbach S., Sicolo S., Kroll P., Duerrschnabel M., Nishiyama N., Kolb U., Albe K., Kleebe H.-J., Riedel R.. High-Pressure Synthesis of Novel Boron Oxynitride B6 N4 O3 with Sphalerite Type Structure. Chem.

Mater. 2015;27(17):5907–5914. doi: 10.1021/acs.chemmater.5b01706. [DOI] [Google Scholar]

20. Missen O. P., Mills S. J., Canossa S., Hadermann J., Nénert G., Weil M., Libowitzky E., Housley R. M., Artner W., Kampf A. R., Rumsey M. S., Spratt J., Momma K., Dunstan M. A.. Polytypism in Mcalpineite: A Study of Natural and Synthetic Cu3 TeO6. Acta Crystallogr., Sect. B:Struct. Sci., Cryst. Eng. Mater. 2022;78(1):20–32. doi: 10.1107/S2052520621013032. [DOI] [PubMed] [Google Scholar]

21. Meagher E. P., Lager G. A.. Polyhedral Thermal Expansion in the TiO2 Polymorphs: Refinement of the Crystal Structures of Rutile and Brookite at High Temperature. Can. Miner. 1979;17(1):77–85. [Google Scholar]

22. De La Flor G., Orobengoa D., Tasci E., Perez-Mato J. M., Aroyo M. I.. Comparison of Structures Applying the Tools Available at the Bilbao Crystallographic Server. J. Appl. Crystallogr. 2016;49(2):653–664. doi: 10.1107/S1600576716002569. [DOI] [Google Scholar]

23. Klar P. B., Krysiak Y., Xu H., Steciuk G., Cho J., Zou X., Palatinus L.. Accurate Structure Models and Absolute Configuration Determination Using Dynamical Effects in Continuous-Rotation 3D Electron Diffraction Data. Nat. Chem. 2023;15(6):848–855. doi: 10.1038/s41557-023-01186-1. [DOI] [PMC free article] [PubMed] [Google Scholar]

24. Gemmi, M. ; Palatinus, L. ; Boullay, P. ; Abrahams, J. P. ; Ben Meriem, A. ; Cordero Oyonarte, E. ; Emerson Agbemeh, V. ; Chintakindi, H. ; Faye Diouf, M. D. ; Filipcik, P. ; Gemmrich Hernandez, L. ; van Genderen, E. ; Hadermann, J. ; Hajizadeh, A. ; Jeriga, B. ; Kolb, U. ; Matinyan, S. ; Passuti, S. ; Santucci, M. ; Suresh, A. ; Pérez, O. ; Tai, C.-W. ; Vypritskaia, A. ; Wang, L. ; Xu, H. ; Zou, X. . Round Robin on Structure Refinement Quality with 3D Electron Diffraction Data. IUCrJ 2025. Submitted. [Google Scholar]

25. Cichocka M. O., Ångström J., Wang B., Zou X., Smeets S.. High-Throughput Continuous Rotation Electron Diffraction Data Acquisition via Software Automation. J. Appl. Crystallogr. 2018;51(6):1652–1661. doi: 10.1107/S1600576718015145. [DOI] [PMC free article] [PubMed] [Google Scholar]

26. Plana-Ruiz S., Krysiak Y., Portillo J., Alig E., Estradé S., Peiró F., Kolb U.. Fast-ADT: A Fast and Automated Electron Diffraction Tomography Setup for Structure Determination and Refinement. Ultramicroscopy. 2020;211:112951. doi: 10.1016/j.ultramic.2020.112951. [DOI] [PubMed] [Google Scholar]

27. Yang T., Xu H., Zou X.. Improving Data Quality for Three-Dimensional Electron Diffraction by a Post-Column Energy Filter and a New Crystal Tracking Method. J. Appl. Crystallogr. 2022;55(6):1583–1591. doi: 10.1107/S1600576722009633. [DOI] [PMC free article] [PubMed] [Google Scholar]

28. Petříček V., Palatinus L., Plášil J., Dušek M.. Jana2020 – a New Version of the Crystallographic Computing System Jana. Z. Kristallogr. Cryst. Mater. 2023;238(7–8):271–282. doi: 10.1515/zkri-2023-0005. [DOI] [Google Scholar]

29. Brázda P., Klementová M., Krysiak Y., Palatinus L.. Accurate Lattice Parameters from 3D Electron Diffraction Data. I. Optical Distortions. IUCrJ. 2022;9(6):735–755. doi: 10.1107/S2052252522007904. [DOI] [PMC free article] [PubMed] [Google Scholar]

30. Passuti S., Varignon J., David A., Boullay P.. Scanning Precession Electron Tomography (SPET) for Structural Analysis of Thin Films along Their Thickness. Symmetry. 2023;15(7):1459. doi: 10.3390/sym15071459. [DOI] [Google Scholar]

31. Yang H., Hazen R. M.. Crystal Chemistry of Cation Order–Disorder in Pseudobrookite-Type MgTi2O5. J. Solid State Chem. 1998;138(2):238–244. doi: 10.1006/jssc.1998.7775. [DOI] [Google Scholar]

32. Smeets S., Zou X., Wan W.. Serial Electron Crystallography for Structure Determination and Phase Analysis of Nanocrystalline Materials. J. Appl. Crystallogr. 2018;51(5):1262–1273. doi: 10.1107/S1600576718009500. [DOI] [PMC free article] [PubMed] [Google Scholar]

33. Hogan-Lamarre P., Luo Y., Bücker R., Miller R. J. D., Zou X.. STEM SerialED: Achieving High-Resolution Data for Ab Initio Structure Determination of Beam-Sensitive Nanocrystalline Materials. IUCrJ. 2024;11(1):62–72. doi: 10.1107/S2052252523009661. [DOI] [PMC free article] [PubMed] [Google Scholar]

34. Bücker R., Hogan-Lamarre P., Mehrabi P., Schulz E. C., Bultema L. A., Gevorkov Y., Brehm W., Yefanov O., Oberthür D., Kassier G. H., Dwayne Miller R. J.. Serial Protein Crystallography in an Electron Microscope. Nat. Commun. 2020;11(1):996. doi: 10.1038/s41467-020-14793-0. [DOI] [PMC free article] [PubMed] [Google Scholar]

35. Rauch E. F., Dupuy L.. Rapid Spot Diffraction Patterns Idendification through Template Matching. Arch. Metall. Mater. 2005;50(1):87–99. [Google Scholar]

36. Rauch E. F., Portillo J., Nicolopoulos S., Bultreys D., Rouvimov S., Moeck P.. Automated Nanocrystal Orientation and Phase Mapping in the Transmission Electron Microscope on the Basis of Precession Electron Diffraction. Z. Kristallogr. 2010;225(2–3):103–109. doi: 10.1524/zkri.2010.1205. [DOI] [Google Scholar]

37. Palatinus L., Brázda P., Jelínek M., Hrdá J., Steciuk G., Klementová M.. Specifics of the Data Processing of Precession Electron Diffraction Tomography Data and Their Implementation in the Program PETS2.0. Acta Crystallogr., Sect. B:Struct. Sci., Cryst. Eng. Mater. 2019;75(4):512–522. doi: 10.1107/S2052520619007534. [DOI] [PubMed] [Google Scholar]

38. Kandiel T. A., Feldhoff A., Robben L., Dillert R., Bahnemann D. W.. Tailored Titanium Dioxide Nanomaterials: Anatase Nanoparticles and Brookite Nanorods as Highly Active Photocatalysts. Chem. Mater. 2010;22(6):2050–2060. doi: 10.1021/cm903472p. [DOI] [Google Scholar]

39. Calatayud D. G., Jardiel T., Peiteado M., Rodríguez C. F., Espino Estévez M. R., Doña Rodríguez J. M., Palomares F. J., Rubio F., Fernández-Hevia D., Caballero A. C.. Highly Photoactive Anatase Nanoparticles Obtained Using Trifluoroacetic Acid as an Electron Scavenger and Morphological Control Agent. J. Mater. Chem. A. 2013;1(45):14358. doi: 10.1039/c3ta12970e. [DOI] [Google Scholar]

40. Horn M., Schwerdtfeger C. F., Meagher E. P.. Refinement of the Structure of Anatase at Several Temperatures. Z. Kristallogr. 1972;136(3–4):273–281. doi: 10.1524/zkri.1972.136.3-4.273. [DOI] [Google Scholar]

41. Guizzardi M., Ghini M., Villa A., Rebecchi L., Li Q., Mancini G., Marangi F., Ross A. M., Zhu X., Kriegel I., Scotognella F.. Near-Infrared Plasmon-Induced Hot Electron Extraction Evidence in an Indium Tin Oxide Nanoparticle/Monolayer Molybdenum Disulfide Heterostructure. J. Phys. Chem. Lett. 2022;13(42):9903–9909. doi: 10.1021/acs.jpclett.2c02358. [DOI] [PMC free article] [PubMed] [Google Scholar]

42. González G. B., Cohen J. B., Hwang J.-H., Mason T. O., Hodges J. P., Jorgensen J. D.. Neutron Diffraction Study on the Defect Structure of Indium–Tin–Oxide. J. Appl. Phys. 2001;89(5):2550–2555. doi: 10.1063/1.1341209. [DOI] [Google Scholar]

43. Selvamani T., Anandan S., Asiri A. M., Maruthamuthu P., Ashokkumar M.. Preparation of MgTi2O5 Nanoparticles for Sonophotocatalytic Degradation of Triphenylmethane Dyes. Ultrason. Sonochem. 2021;75:105585. doi: 10.1016/j.ultsonch.2021.105585. [DOI] [PMC free article] [PubMed] [Google Scholar]

44. Smeets, S. ; Wang, B. ; Hogenbirk, E. . Instamatic-Dev/Instamatic: 1.7.0, 2021.

45. Rodríguez-Carvajal J.. Recent Advances in Magnetic Structure Determination by Neutron Powder Diffraction. Phys. B. 1993;192(1–2):55–69. doi: 10.1016/0921-4526(93)90108-I. [DOI] [Google Scholar]

46. Roisnel T., Rodríquez-Carvajal J.. WinPLOTR: A Windows Tool for Powder Diffraction Pattern Analysis. Mater. Sci. Forum. 2001;378–381:118–123. doi: 10.4028/www.scientific.net/MSF.378-381.118. [DOI] [Google Scholar]

47. Momma K., Izumi F.. VESTA 3 for Three-Dimensional Visualization of Crystal, Volumetric and Morphology Data. J. Appl. Crystallogr. 2011;44(6):1272–1276. doi: 10.1107/S0021889811038970. [DOI] [Google Scholar]

48. Järvinen M.. Application of Symmetrized Harmonics Expansion to Correction of the Preferred Orientation Effect. J. Appl. Crystallogr. 1993;26(4):525–531. doi: 10.1107/S0021889893001219. [DOI] [Google Scholar]

49. Palatinus L., Chapuis G.. SUPERFLIP – a Computer Program for the Solution of Crystal Structures by Charge Flipping in Arbitrary Dimensions. J. Appl. Crystallogr. 2007;40(4):786–790. doi: 10.1107/S0021889807029238. [DOI] [Google Scholar]